Rev. Adv. Mater. Sci. 52 (2017) 61-69

INFLUENCE OF ADDITIONAL DEFORMATION ON MICROSTRUCTURE, MECHANICAL AND ELECTRICAL PROPERTIES OF Al-Mg-Si ALLOY PROCESSED BY HIGH PRESSURE TORSION

A.M. Mavlyutov[1], T.S. Orlova[1,2], T.A. Latynina[1], I.A. Kasatkin[3], M.Yu. Murashkin[3,4] and R.Z. Valiev[3,4]

[1]Saint Petersburg National Research University of Information Technologies, Mechanics and Optics, Kronverksky Pr. 49, St. Petersburg 197101 Russia
[2]Ioffe Physical-Technical Institute of the Russian Academy of Sciences, Politekhnicheskaya str. 26, St. Petersburg 194021 Russia
[3]Saint Petersburg State University, Universitetskiy Pr. 28, St. Petersburg 198504 Russia
[4]Institute of Physics of Advanced Materials, Ufa State Aviation Technical University, K. Marx str. 12, Ufa 450000 Russia

Received: July 21, 2017

Abstract. This paper presents a study on the influence of minor additional torsional strain by $\Delta\gamma \leq 0.036$ at room temperature on the microstructure, mechanical and electrical properties of the ultrafine-grained (UFG) alloy of the Al-Mg-Si system that has been preliminarily subjected to complex treatment by severe plastic deformation at room and elevated temperatures (with a total strain $\gamma = 6.54$). The optimal regime of additional strain ($\Delta\gamma \approx 0.024$) is reported, showing the best combination of strength and electrical properties, particularly an increase in the ultimate tensile strength by ~14% while maintaining the electrical conductivity at ~56% IACS. This is achieved by introducing additional dislocation density while preserving other microstructural parameters such as grain size, the volume and distribution of secondary phases, the distribution of grain boundaries on misorientations. The contributions of various mechanisms to the hardening and charge scattering are estimated as a function of the value of $\Delta\gamma$ and the estimates are in good agreement with the experimental data when $\Delta\gamma \leq 0.024$ and most likely indicate the start of dissolution of Mg_2Si secondary phase nanoparticles at larger additional strain ($\Delta\gamma \approx 0.036$), which leads to additional strengthening but sacrifices electrical conductivity.

1. INTRODUCTION

Mechanical strength, corrosion resistance, high electrical conductivity and thermal stability are the most important properties of wires used in overhead power lines. The most common conductor applied for electric power transmission today is steel-aluminum wire that consists of a steel core and aluminum cladding [1–3]. The steel core provides the necessary mechanical strength to the wire, whereas the commercially pure aluminum cladding is what conducts electricity. This design has a number of drawbacks such as difficulty in production and installation as well as high specific weight of the wires. In addition, low corrosion resistance of the steel core and a twofold difference in the coefficients of thermal expansion of steel and aluminum cause rapid failure of in-service wires [2]. Recent years have witnessed active development of the technologies to increase strength of aluminum that will make it possible to refuse the steel core and eliminate the problems above [1–4].

Corresponding author: T.S. Orlova, e-mail: orlova.t@mail.ioffe.ru

© 2017 Advanced Study Center Co. Ltd.

Traditionally, the addition of alloying elements to aluminum is the principal method to improve its strength characteristics. For the alloy of the Al-Mg-Si system, further increase in the strength is possible through special heat treatment (according to the international T6 classification) that results in the formation of particles of hardening secondary phases [5]. Another method to increase the strength is deformation processing of the alloys by rolling, drawing, etc. All the above strengthening methods are based on introducing a large amount of crystal structure defects (grain boundaries, dislocations, impurity atoms, secondary phase particles) into the metal microstructure. However, this leads to an increase in the electrical resistivity of the alloys due to the scattering of conduction electrons by impurity atoms in solid solution, their clustering and crystal structure defects [6]. As a result, high strength and high electrical conductivity cannot be simultaneously achieved by means of traditional treatment techniques.

Severe plastic deformation (SPD) techniques make it possible to significantly increase the strength of the Al-based alloys by forming a unique microstructure consisting of nano-sized grains and containing a high concentration of defects [7]. In recent works [8–10] the influence of high pressure torsion (HPT) on the microstructure and functional properties of the Al 6201 alloy (a widely used electrotechnical alloy of the Al-Mg-Si system) was studied. As was shown, HPT at room temperature (RT) results in a considerable grain refinement down to 130 nm and further processing by HPT at a temperature of 403–503K promotes dynamic aging, i.e. the formation of Mg_2Si secondary phase nanoparticles that additionally contribute to hardening. Dynamic aging is accompanied by purification of the aluminum matrix from the Mg and Si atoms, which provides a marked increase in electrical conductivity of the alloy [8,9]. Despite the good combination of strength and electrical properties achieved in the material, further increase in strength while maintaining high electrical conductivity still remains a very important problem of materials science in the field of nanostructured electrotechnical Al alloys. A new approach was suggested in [10] to improve strength through increasing the dislocation density by minor additional plastic deformation. As was demonstrated, additional processing through 0.25 turn of HPT at RT ($\Delta\gamma\approx0.012$) does not generally affect the parameters of the microstructure formed but leads to the increased dislocation density, thus resulting in additional improvement of microhardness by 15% while maintaining high electrical conductivity [10].

This paper reports a complex study carried out to further develop the approach suggested in [10] to establish the influence of the value of additional plastic deformation on the microstructural evolution and resulting properties (conventional yield stress, ultimate tensile strength and electrical conductivity) of the UFG Al 6201 alloy subjected to preliminary high pressure torsion. The microstructural parameters determined in this work serve as the basis to evaluate the change of different contributions to hardening and charge scattering that are compared with the experimental data. The regime of additional deformation providing the optimal combination of high strength and electrical conductivity is determined.

2. MATERIAL AND EXPERIMENTAL PROCEDURES

Electrotechnical Al 6201 alloy was chosen as the material of interest for this study with the following chemical composition: 0.81Mg; 0.79Si; 0.09Fe; 0.1Cu; 0.02Zn; 0.02(Ti+V+Cr+Mn); balance Al (wt.%). The disk-shaped samples 1.5 mm thick were cut from the 20 mm diameter rod initially processed by continuous casting and rolling [11,12]. The samples were subjected to homogenization annealing at a temperature of 823K during 2 h followed by quenching in water. Then the samples were processed by HPT technique [7,13] with the following regime: 1 turn (n=1) of HPT at RT under a pressure of 6 GPa and further HPT at 503K under a pressure of 6 GPa, n=20 (regime A, Table 1). After HPT processing the true strain at the distance of 5 mm from the disk center was $\gamma\approx6.54$ [13]. Such HPT regime was used for providing good combination of

Table 1. HPT processing regimes for the Al 6201 alloy. $\Delta\gamma$ is the value of additional true strain.

	processing stage 1	processing stage 2	$\Delta\gamma$
Regime A	HPT at RT, n=1 + HPT at 503K, n=20	-	-
Regime B	the same processing	HPT at RT, n=0.25	0.012
Regime C	the same processing	HPT at RT, n=0.5	0.024
Regime D	the same processing	HPT at RT, n=0.75	0.036

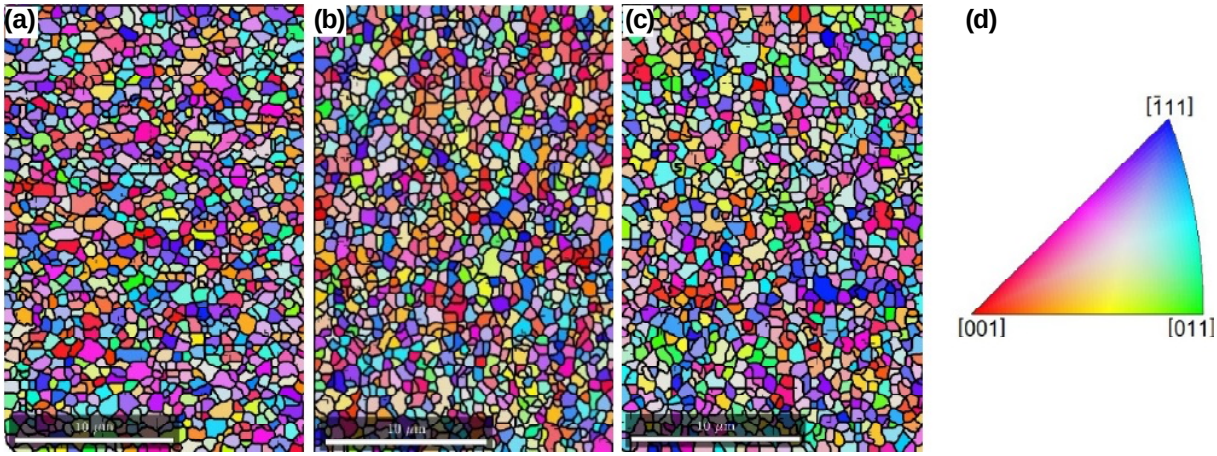

Fig. 1. EBSD maps of the Al 6201 alloy processed by regimes A (a), B (b), D (c) and the inverse pole figure coloring for distribution of grain orientation (d).

high strength and electrical conductivity [8,10] and these very samples were applied to further investigate the influence of additional strain on the microstructure and resulting properties. For this purpose, a number of samples processed according to regime A were additionally subjected to HPT at RT with n=0.25, 0.5 and 0.75 (regimes B, C and D, Table 1), whereas the additional true strain constituted $\Delta\gamma\approx$0.012, 0.024 and 0.036, respectively (Table 1).

Microstructure of the obtained samples was studied by electron backscattering diffraction (EBSD) and X-ray diffraction (XRD) analysis. The EBSD studies were performed using the scanning electron microscope Zeiss Merlin with a scan step of 0.2 μm. The diffraction patterns were indexed using seven Kikuchi bands. At least 2000 grains were analyzed to determine the distributions of grains on size and grain boundaries between the adjacent grains on their misorientation angle (θ). The area of each grain determined during the EBSD mapping was approximated by the area of a circle, the diameter of which was taken as a grain size [14]. The average grain size (d_{av}) was calculated from the obtained distributions of grains on size. Grain boundaries with misorientation angle $\theta \geq 15°$ were referred to high-angle grain boundaries (HAGBs), the percentage of HAGBs is further denoted as $f_{\geq 15}$. XRD measurements were taken on the Bruker D8 DISCOVER diffractometer in the regime of symmetric φ-2φ scanning with a parallel radiation beam CuKα (40 kV, 40 mA). The scanning step was $\Delta 2\varphi$=0.02 and exposition time – 0.5 s. The Pauli analysis method using «TOPAS 5.0» software was applied to determine lattice parameter (a), average size of coherent-scattering regions (D_{XRD}) and elastic microdistortion level ($\langle\varepsilon^2\rangle^{1/2}$). The dislocation density L_{dis} was estimated from the data obtained in accordance with [15]:

$$L_{dis} = 2\sqrt{3}\left\langle \varepsilon^2 \right\rangle^{1/2} \Big/ D_{XRD} b, \qquad (1)$$

where b is the Burgers vector.

Vickers microhardness (H_V) was measured using a Shimadzu HMV-G tester with a load of 1 N during 15 s. Each sample was tested at least 15 times, the indentations being performed along the chord at a distance of 5 mm from the disk center. The samples for mechanical tests were cut from the HPT-processed disks with the electric-spark machine in the shape of blades with a gauge width of 2 mm and a gauge length of 6 mm. The cutting scheme and sample configuration are presented in [16]. The uniaxial tensile test was performed on a Shimadzu AG-XD Plus machine with a constant strain rate of $5\cdot10^{-4}$ s^{-1}. Sample straining was recorded using a TRViewX 55S video extensometer. At least 3 samples were tested for each state. The conventional yield stress ($\sigma_{0.2}^{exp}$) corresponding to 0.2% strain, ultimate tensile strength (σ_{UTS}) and relative elongation to failure (δ) were determined from the stress-strain diagrams obtained.

Electrical resistivity at 293K (ρ_{293}^{ec}) was measured by the eddy current method with a relative error of ± 2% following the international standard ASTM E1004. Considering that the degree of conduction electron scattering from thermal vibrations in the lattice considerably reduces and relative effect of the influence of microstructure parameters on the resistivity increases, additional measurements were performed using a four-probe method at 77K (ρ_{77}), as well as at a number of intermediate temperatures in a range of 100–300K. The sample temperature was controlled by a silicon diode with an accuracy of 0.03K. For the four-probe method the meas-

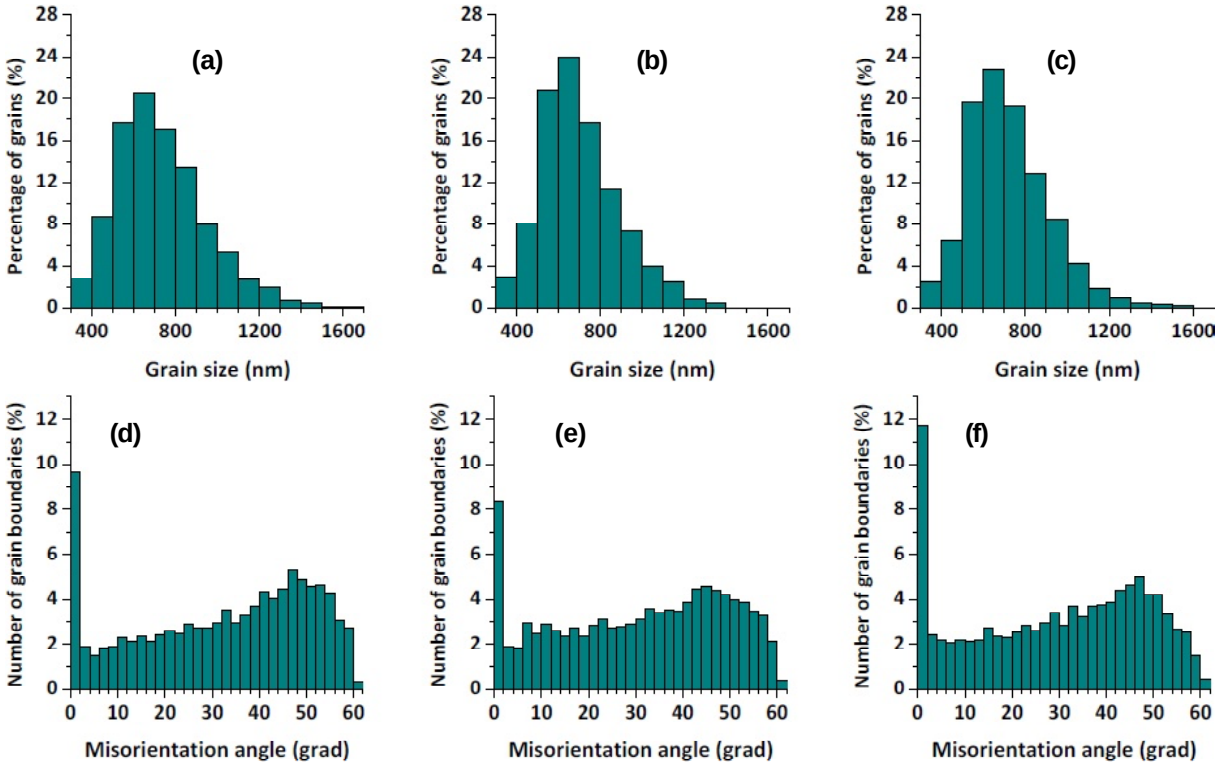

Fig. 2. Size distribution of grains (a, b, c) and distribution of grain boundaries on misorientation angles (d, e, f) for the Al 6201 alloy processed by regimes A (a, d), B (b, e) and D (c, f).

Table 2. Microstructural parameters of the Al 6201 alloy. a – lattice parameter, $\langle\varepsilon^2\rangle^{1/2}$ – crystal lattice microdistortion, D_{XRD} – average size of coherent-scattering regions, d_{av} – average grain size, $f_{\geq 15}$ – fraction of grain boundaries with misorientation angle $\theta \geq 15^o$, L_{dis} – dislocation density.

Processing regime	a, Å	$\langle\varepsilon^2\rangle^{1/2}$, %	D_{XRD}, nm	d_{av}, nm	$f_{\geq 15}$, %	L_{dis}, m^{-2}
A	4.0505±0.0001	0.016±0.0003	440±90	738±211	78	$4.5 \cdot 10^{12}$
B	4.0505±0.0002	0.038±0.0003	240±80	708±184	76	$1.9 \cdot 10^{13}$
C	4.0504±0.0002	0.033±0.0003	220±60	662±195	74	$1.8 \cdot 10^{13}$
D	4.0505±0.0002	0.038±0.0003	270±20	723±187	74	$1.8 \cdot 10^{13}$

uring error of resistivity was <2%. The obtained data were used for linear approximation to determine the resistivity at 293K (ρ_{293}). Electrical resistivity measurements by a four probe method are described with more details in [17,18].

3. EXPERIMENTAL RESULTS

3.1. Microstructure evolution

Microstructure was analyzed by electron backscattering diffraction (EBSD) and X-ray diffraction (XRD). Fig. 1 demonstrates the EBSD maps of the samples processed following the regime A (Fig. 1a), B (Fig. 1b), and D (Fig. 1c). An HPT regime A leads to the formation of UFG structure with equiaxed grains. The distribution of grains on their size is presented in Fig. 2a. Average grain size (d_{av}) is equal to ~740 nm, ~78% of GBs having high-angle misorientation (Fig. 2d). Additional straining of UFG samples following the regimes B, C, and D produces no considerable effect on d_{av} and $f_{\geq 15}$ (Fig.1 and 2). For example, maximum additional strain $\Delta\gamma \approx 0.036$ (regime D) results in $d_{av} \approx 725$ nm and $f_{\geq 15} \approx 74\%$ (Table 2).

The microstructural parameters determined by XRD analysis are presented in Table 2: the lattice parameter (a), average size of coherent-scattering regions (D_{XRD}), crystal lattice microdistortions ($\langle\varepsilon^2\rangle^{1/2}$) and dislocation density (L_{dis}) for the samples studied. The values of parameter a for all the samples differ from each other within the measurement error (4.0505±0.0001 Å) and are close in mag-

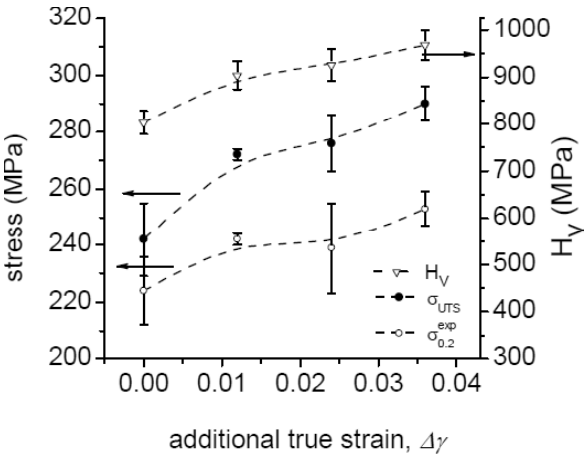

Fig. 3. Dependence of microhardness H_V, conventional yield stress $\sigma_{0.2}^{exp}$ and ultimate tensile strength σ_{UTS} of the Al 6201 alloy on the value of additional strain $\Delta\gamma$.

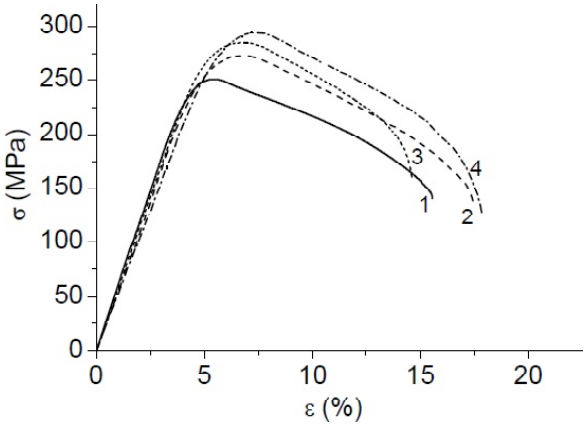

Fig. 4. Stress-strain curves for the Al 6201 alloy processed by regimes A (*1*), B (*2*), C (*3*), and D (*4*).

nitude to the lattice parameter of coarse-grained pure aluminum (4.0495 Å [19]). Additional straining by $\Delta\gamma\approx0.012$ (following the regime B) increases crystal lattice microdistortions and also reduces D_{XRD} from ~440 to ~240 nm (Table 2). These parameters practically remain the same with an increase of additional strain. As a result of additional strain $\Delta\gamma\approx0.012$ during processing by regime B, the dislocation density increases by a factor of ~4, $L_{dis}\approx1.9\cdot10^{13}$ m^{-2}. Further increase of strain when processing by regimes C and D has no considerable relevance to the value of L_{dis}.

3.2. Mechanical and electrical properties

Fig. 3 shows the dependence of the Vickers microhardness (H_V) on the value of additional strain $\Delta\gamma$. The microhardness of a sample processed by regime A ($\Delta\gamma$=0) is ~803 MPa. Additional straining of the UFG samples by $\Delta\gamma\approx0.012$, 0.024 and 0.036 contributes to an increase in H_V to ~905, ~925 and ~970 MPa, respectively (Table 3).

Fig. 4 presents the results of mechanical tensile tests of Al 6201 samples processed by regimes A–D. The sample subjected to regime A (curve 1) has conventional yield stress $\sigma_{0.2}^{exp}\approx224$ MPa, ultimate tensile strength $\sigma_{UTS}\approx242$ MPa and elongation to failure $\delta\approx14\%$ (Table 3). With additional strain $\Delta\gamma$=0.012–0.036, the character of change in ultimate tensile strength and conventional yield stress is similar to that in microhardness (Fig. 3). The maximum yield stress and ultimate tensile strength to ~253 and ~290 MPa, respectively (curve 4 in Fig. 4 and Table 3) are observed at $\Delta\gamma\approx0.036$, whereas elongation to failure equals to $\delta\approx15\%$.

The results of resistivity measurements by the eddy current (ρ_{293}^{ec}) and four-probe methods at 293K (ρ_{293}) are shown in Fig. 5a (curve 1 and curve 2, respectively). It is worth noting the correlations between measurement results obtained by different methods are strong. In the samples processed by regime A, electrical resistivity constitutes $\rho_{293}^{ec}\approx30.63$ nΩm, which corresponds to conductivity $\omega\approx56.3\%$ IACS (Table 3). As is seen, additional strain

Table 3. Mechanical and electrical properties of the Al 6201 alloy. $\sigma_{0.2}^{exp}$ – conventional yield stress, σ_{UTS} – ultimate tensile strength, H_V – microhardness, δ – relative elongation to failure, ρ_{77} – electrical resistivity at 77K, ρ_{293}^{ec} – electrical resistivity at 293K, ω – specific electrical conductivity.

Processing regime	$\sigma_{0.2}^{exp}$, MPa	σ_{UTS}, MPa	H_V, MPa	δ,%	ρ_{77}, nΩm	ρ_{293}^{ec}, nΩm	ω, % IACS
A	224±12	242±13	803±24	14±2	5.93	30.63	56.3
B	242±2	272±2	904±30	14±1	6.42	30.82	55.9
C	239±16	276±10	926±35	13±1	6.10	30.82	55.9
D	253±6	290±6	968±32	15±1	6.58	31.26	55.2

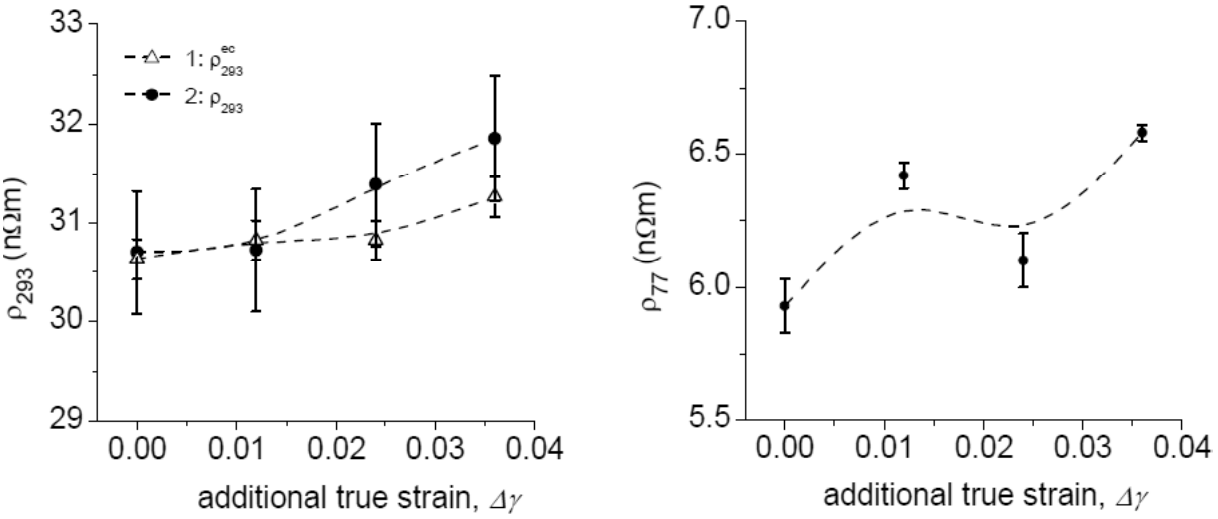

Fig. 5. Dependence of electrical resistivity at 293K (a) and 77K (b) on the value of additional strain $\Delta\gamma$.

$\Delta\gamma\approx0.012$–0.024 almost does not affect electrical resistivity, and with $\Delta\gamma\approx0.036$ the resistivity slightly increases by ~2% ($\rho_{293}^{ec}\approx31.26$ nΩm). In order to estimate the dependence of electrical resistivity on the parameters of resulting microstructure, it is reasonably to carry out the measurements at cryogenic temperatures that substantially eliminate the effect of thermal lattice vibrations. Fig. 5b shows the results of resistivity measurements at 77K, when the resistivity behavior remains the same as at 293K, while the change in the resistivity is ~11% for $\Delta\gamma\approx0.036$. The data obtained are also provided in Table 3.

4. DISCUSSION

The yield stress in metals can be represented as a sum of contributions from different mechanisms to strengthening [20–22]:

$$\sigma_{0.2} = \sigma_0 + \sigma_{GB} + \sigma_{SS} + \sigma_{Or} + \sigma_{dis}, \quad (2)$$

where σ_0 is the friction stress of crystal lattice, σ_{GB} is the grain boundary hardening determined by the Hall-Petch relation [23,24], σ_{ss} is the solid-solution hardening, σ_{Or} is the Orowan hardening due to the presence of secondary phase nanoparticles [25], σ_{dis} is the dislocation (strain) hardening.

As we earlier demonstrated [10], additional straining of the UFG Al 6201 alloy by $\Delta\gamma\approx0.012$ does not affect the size and distribution of secondary phase particles, as well as the concentration of impurity atoms in solid solution, whereas the change in conventional yield stress at such degree of additional strain is related to only the change in grain boundary and dislocation hardening contributions:

$$\delta\sigma_{0.2} = \delta\sigma_{GB} + \delta\sigma_{dis}. \quad (3)$$

Assuming the same scenario for $\Delta\gamma$=0.024–0.036, let us estimate how the conventional yield stress changes depending on the value of additional strain. The microstructural parameters obtained (Table 3) serve as a basis to estimate these hardening contributions according to the relations [23,24,26]:

$$\sigma_{GB} = Kd_{av}^{-1/2}, \quad (4)$$

$$\sigma_{dis} = M\alpha GbL_{dis}^{1/2}, \quad (5)$$

where: K=0.1 MPa m^{-1} is the Hall-Petch coefficient [27], d_{av} is the average grain size, M=3.06 is the Taylor factor [26], α=0.33 is the dislocation interaction parameter [28], G = 26 GPa is the shear modulus, b=2.86 Å is the Burgers vector, L_{dis} is the dislocation density according to the XRD data.

Fig. 6 shows the dependences of the change in the conventional yield stress after additional strain on the value of this strain, obtained experimentally (curve 1) and calculated from equations (3)–(5) (curve 2). As is seen, the results of estimated value $\delta\sigma_{0.2}$ at $\Delta\gamma$=0.024–0.036 considerably differ from the experimental data $\delta\sigma_{0.2}^{exp}$ (Table 4). Such discrepancy is, first of all, likely due to the fact that the hardening contribution from some grain boundaries with low misorientations is of dislocation character and does not bring to grain boundary hardening. Then according to [20] the contribution of grain boundary hardening is as follows:

$$\sigma_{GB} = K\sqrt{(1-f_\theta)/d_{av}}, \quad (6)$$

where f_θ is the fraction of grain boundaries with misorientations lower than a certain critical angle

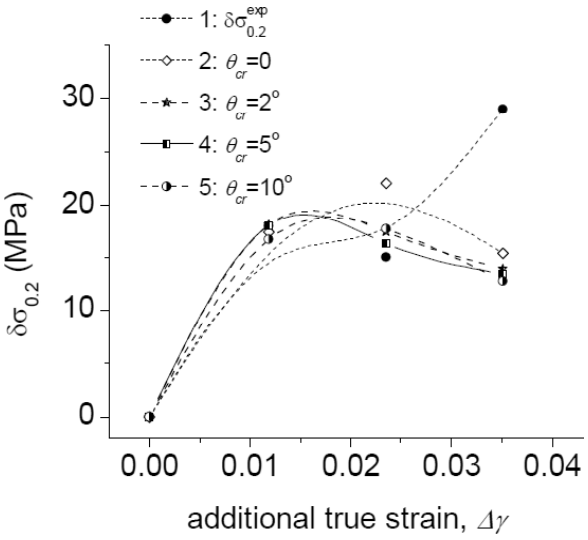

Fig. 6. Change in conventional yield stress obtained experimentally $\delta\sigma_{0.2}^{exp}$ (curve 1), calculated theoretically without (curve 2) and with considering the fraction of dislocation GBs with misorientation angles less than θ_{cr}=2, 5, and 10° (curves 3, 4, and 5, respectively), which do not participate in grain boundary hardening, as a function of the value of additional strain $\Delta\gamma$.

θ_{cr} that do not contribute to grain boundary hardening. Misorientations 2, 5, and 10° were taken as possible values of θ_{cr}. The corresponding parameter f_θ was determined based on GB distribution on misorientations as measured by EBSD method (Figs. 2d-2f). Grain boundaries with misorientation lower than θ_{cr} were referred to dislocation GBs, the strengthening contribution from which is described by dislocation hardening. Eqs. (3), (5), and (6) were used to estimate $\delta\sigma_{0.2}$ (curves 3, 4, and 5, Fig. 6) for the selected values of θ_{cr}=2, 5, and 10°. As is seen in Fig. 6, a good correlation between the experimental and calculated results for additional strain $\Delta\gamma\leq0.024$ is observed for the parameter θ_{cr}=5° (curve 4). At larger additional strain $\Delta\gamma\approx0.036$, there is a considerable difference (by ~15 MPa) between experimental $\delta\sigma_{0.2}^{exp}$ and calculated results for all values of θ_{cr}, which is most likely due to the presence of additional strengthening mechanism in this case. According to [29,30] SPD of some alloys may lead to strain-induced dissolution of the secondary-phase particles. Presumably, additional strain $\Delta\gamma\approx0.036$ resulted in partial dissolution of Mg_2Si nanoparticles and a slight increase in the concentration of Mg and Si atoms in the aluminum matrix, which caused the experimentally observed additional hardening. As will be shown below, this assumption is in good agreement with the results of electrical resistivity change at $\Delta\gamma\approx0.036$.

As is known, the factors that contribute to hardening lead to an increase in electrical resistivity. According to Matthiessen's rule [6,27], electrical resistivity of alloy is equal to the sum of contributions from different scattering mechanisms that do not affect each other:

$$\rho^{alloy} = \rho^{pure} + N_v\Delta\rho^{vac} + L_{dis}\Delta\rho^{disl} + S_{GB}\Delta\rho^{GB} + \sum_i C_i^{sol}\Delta\rho_i^{sol}, \quad (7)$$

where ρ^{pure} (Ωm) is the electric resistivity of a single-crystalline defect-free metal, $\Delta\rho^{vac}$ (Ωm/at.%), $\Delta\rho^{disl}$ =2.7·10^{-25} Ωm^3 [31], $\Delta\rho^{GB}$ =2.6·10^{-16} Ωm^2 [31] are the contributions from unit vacancy concentration, unit densities of dislocations and grain boundaries, respectively, $\Delta\rho_i^{sol}$ (Ωm/at.%) is the contribution from unit concentration of *i*-th impurity in the solid solution, N_V (at.%) is the vacancy concentration, L_{disl} (m^{-2}) is the dislocation density, S_{GB} (m^{-1}) is the bulk density of GBs, C_i^{sol} (at.%) is the concentration of *i*-th solute atom.

Vacancies in the HPT-processed Al alloys have a negligible contribution to the electrical resistivity because they are very quickly annealed in the sam-

Table 4. Assessment of changes in conventional yield stress $\delta\sigma_{0.2}$ of the Al 6201 alloy due to varying contributions of dislocation hardening $\delta\sigma_{dis}$ and grain boundary hardening $\delta\sigma_{GB}$, θ_{cr} – the maximum misorientation angle of grain boundaries not taking part in grain boundary hardening. $\delta\sigma_{0.2}^{exp}$ – the conventional yield stress change obtained experimentally, $\Delta\gamma$ – additional true strain.

Processing regime	$\delta\sigma_{dis}$, MPa	θ_{cr}=0°		θ_{cr}=2°		θ_{cr}=5°		θ_{cr}=10°		$\delta\sigma_{0.2}^{exp}$, MPa	$\Delta\gamma$
		$\delta\sigma_{GB}$, MPa	$\delta\sigma_{0.2}$, MPa	$\delta\sigma_{GB}$, MPa	$\delta\sigma_{0.2}$, MPa	$\delta\sigma_{GB}$, MPa	$\delta\sigma_{0.2}$, MPa	$\delta\sigma_{GB}$, MPa	$\delta\sigma_{0.2}$, MPa		
B	15	2	17	3	18	3	18	2	17	18	0.012
C	14	8	22	3	17	2	16	4	18	15	0.024
D	14	1	15	0	14	-1	13	-1	13	29	0.036

ples even at room temperature [31]. The EBSD and XRD analyses make it possible to reveal the resistance gain due to the change in the average grain size and dislocation density at $\Delta\gamma\approx0.036$ (processing by regime D). It is estimated that the change in the average grain size from 740 to 725 nm leads to an increase in resistivity by ~0.02 nΩm and the growth of dislocation density from $4.5\cdot10^{12}$ to $1.8\cdot10^{13}$ m^{-2} – by ~0.004 nΩm. The calculated values are considerably lower than that experimental $\Delta\rho_{77}\approx0.65$ nΩm. For this reason, the resistivity change at $\Delta\gamma\approx0.036$ is most likely due to an increase in the impurity concentration in solid solution. As estimated, an increase in the concentration of Mg by ~0.12 wt.% and, therefore, of Si by ~0.07 wt.% due to partial dissolution of Mg_2Si secondary phase particles would provide the growth of the electrical resistivity by the experimentally observed value $\Delta\rho_{77}\approx0.65$ nΩm. Then the corresponding change in the contribution of solid solution hardening may be estimated as [32]:

$$\delta\sigma_{ss} = \sum_i k_i (\delta c_i)^{2/3}, \quad (8)$$

where δc_i (wt.%) is the change in the concentration of *i*-th alloying element, k_{Mg} = 29 MPa/wt.%$^{2/3}$, k_{Si}=66.3 MPa/wt.%$^{2/3}$ [32].

According to (8) $\delta\sigma_{ss}\approx25$ MPa, taking into account $\delta\sigma_{ss}$, $\delta\sigma_{0.2}$ can be estimated as:

$$\delta\sigma_{0.2} = \delta\sigma_{GB} + \delta\sigma_{dis} + \delta\sigma_{ss}, \quad (9)$$

According to (5)–(9) and noting that θ_{cr}=5°, we obtain $\delta\sigma_{0.2}\approx30$ MPa, which agrees well with the experimental value $\delta\sigma_{0.2}^{exp}\approx29$ MPa.

The evaluation results show that during additional straining of the UFG Al 6201 alloy by $\Delta\gamma\approx0.036$ (processing by regime D) the process of dissolution of the Mg_2Si particles most likely starts, which leads to an increase in the yield stress and a decrease in the electrical conductivity of the samples. Thus, additional straining $\Delta\gamma\approx0.024$ (regime C) may be considered as the most successful for achieving an optimal combination of high strength and high electrical conductivity in the Al 6201 alloy.

5. CONCLUSIONS

In this work the influence of additional torsional strain by $\Delta\gamma\leq0.036$ at room temperature on the mechanical and electrical properties of the UFG Al 6201 alloy preliminarily subjected to HPT at RT and 503K has been studied.

It has been experimentally shown that additional straining of the samples with the UFG structure by $\Delta\gamma\approx0.024$ leads to an increase in the dislocation density by a factor of ~4 without changing other microstructural parameters, which provides the enhancement of yield stress by ~14% while preserving an electrical conductivity of 56% IACS.

Additional straining the UFG alloy by $\Delta\gamma\approx0.036$ provides an increase the ultimate tensile strength to ~290 MPa with a small decrease in the electrical conductivity (55.2% IACS). Analysis of the contributions to hardening and charge scattering has showed that in this case, the process of dissolution of Mg_2Si secondary phase particles is most likely to occur, leading to an increase in impurity concentration in solid solution, which is the reason for the observed increase in strength and decrease in electrical conductivity.

ACKNOWLEDGMENTS

X-ray diffraction studies were provided using the equipment of the Resource Centre for X-ray Diffraction Methods of Research of Saint Petersburg State University.

EBSD analyses were conducted on the equipment of the Interdisciplinary Resource Centre for Nanotechnology of Saint Petersburg State University.

AMM and TSO thank the Ministry for Education and Science of the Russian Federation for support (Project No 3.3194.2017/4.6)

REFERENCES

[1] D.I. Beliy // *Kabeli i Provoda* **332** (2012) 8, in Russian.

[2] A.S. Kuvshinov // *Kabeli i Provoda* **345** (2014) 14, in Russian.

[3] V.V. Loparev and Yu.V. Obraztsov // *Kabeli i Provoda* **349** (2014) 9, in Russian.

[4] K.Sh. Mangutov and D.P. Pigarev // *Kabeli i Provoda* **349** (2014) 17, in Russian.

[5] L.A. Vorontsova, V.V. Maslov and I.B. Peshkov, *Aluminum and Aluminum-based alloys in electrical products* (Energiya, Moscow, 1972), in Russian.

[6] P.L. Rossiter, *The Electrical Resistivity of Metals and Alloys* (Cambridge University Press, Cambridge, 2003).

[7] R.Z. Valiev, R.K. Islamgaliev and I.V. Alexandrov // *Prog. Mater. Sci.* **45** (2000) 103.

[8] R.Z. Valiev, M.Yu. Murashkin and I. Sabirov // *Scripta Mater*. **76** (2014) 13.

[9] E.V. Bobruk, M.Yu. Murashkin,V.U. Kazykhanov and R.Z. Valiev // *Rev. Adv. Mater. Sci*. **31** (2012) 109.

[10] A.M. Mavlyutov, I.A. Kasatkin, M.Yu. Murashkin, R.Z. Valiev and T.S. Orlova // *Physics of the Solid State* **57** (2015) 2051.
[11] *Machine for the continuous casting of metal rods*, US 2659948 A 24.11.1953.
[12] *Method of fabricating aluminum alloy rod*, US 3670401 A 20.06.1972.
[13] A.P. Zhilyaev and T.G. Langdon // *Prog. Mater. Sci.* **53** (2008) 893.
[14] F.J. Humphreys // *J. Microsc*. **195** (1999) 170.
[15] G.K. Williamson and R.E. Smallman // *Phil. Mag*. **1** (1956) 34.
[16] A.M. Mavlyutov, T.A.Latynina, M.Yu. Murashkin, R.Z. Valiev and T.S. Orlova // *Physics of the Solid State* **10** (2017) 1949.
[17] T.S. Orlova, A.M. Mavlyutov, A.S. Bondarenko, I.A. Kasatkin, M.Yu. Murashkin and R.Z. Valiev // *Phil. Mag*. **96** (2016) 2429.
[18] A.M. Mavlyutov, A.S. Bondarenko, M.Yu. Murashkin, E.V. Boltynjuk, R.Z. Valiev and T.S. Orlova // *JALCOM* **698** (2017) 539.
[19] S.S. Gorelik, L.N. Rastorguev and Yu.A. Skakov, *X-ray and electron optical analysis* (Metallurgiya, Moscow, 1970), In Russian.
[20] N. Kamikawa, X. Huang, N. Tsuji and N. Hansen // *Acta Mater*. **57** (2009) 4198.
[21] H. Asgharzadeh, A. Simchi and H. S. Kim // *Mater. Sci. Eng. A* **528** (2011) 3981.
[22] H. Asgharzadeh, A. Simchi and H. S. Kim // *Metall. Mater. Trans. A* **42** (2011) 816.
[23] E.O. Hall // *Proc. Phys. Soc. B* **64** (1951) 747.
[24] N. J. Petch // *J. Iron. SteelInst* **174** (1953) 25.
[25] L.M. Brown and R.K. Ham, In: S*trengthening Methods in Crystals*, ed. By A. Kelly and R.B Nicholson (Applied Science, London, 1971), p. 9.
[26] N. Hansen and X. Huang // *Acta Mater.* **46** (1998) 1827.
[27] G.E. Totten and D.S. MacKenzie, *Handbook of Aluminium* (Marcel Dekker, New York, 2003).
[28] F.R.N. Nabarro, Z.S. Basinski and D.B. Holt // *Adv. Phys.* **13** (1964) 193.
[29] I.G. Brodova, I.G. Shirinkina and O.V. Antonova // *Phys. Met. Metall*. **104** (2007) 281.
[30] G. Sha, Y.B. Wang, X.Z. Liao, Z.C. Duan, S.P. Ringer and T.G. Langdon // *Acta M.* **57** (2009) 3123.
[31] Y. Miyajama, Sh.-Ya. Komatsu, M. Mitsuhara, S. Hata, H. Nakashima and N. Tsuji // *Phil. Mag*. **90** (2010) 4475.
[32] O.R. Myhr, O. Grong and S.J. Andersen // *Acta Mater*. **49** (2001) 65.